quality compared to conventional ultrasound. Clin Imaging. 2001;25:379–84.
15. Krücker JF, Meyer CR, LeCarpentier GL, et al. 3D spatial compounding of ultrasound imaging using image-based nonrigid registration. Ultrasound Med Biol. 2000;26:1475–88.
16. Moskalik A, Carson PL, Meyer CR, et al. Registration of 3-dimensional compound ultrasound scans of the breast for refraction and motion correction. Ultrasound Med Biol. 1995;21:769–78.
17. Weinstein SP, Conant EF, Sehgal C. Technical advances in breast ultrasound imaging. Semin Ultrasound CT MR. 2006;27:273–83.
18. Hossack JA, Hayward G. Finite-element analysis of 1–3 composite transducers. IEEE Trans Ultrason Ferroelect Freq Control. 1991;38:618–29.
19. Lerch R. Simulation of piezoelectric devices by two- and three-dimensional finite elements. IEEE Trans Ultrason Ferroelect Freq Control. 1990;37:233–47.

ORIGINAL ARTICLE

ACTA RADIOLOGICA

Diffusion tensor MRI of the kidney at 3.0 and 1.5 Tesla

Aki Kido[1], Masako Kataoka[1,2], Akira Yamamoto[1], Yuji Nakamoto[1], Shigeaki Umeoka[1], Takashi Koyama[1], Yoji Maetani[1], Hiroyuki Isoda[1], Ken Tamai[1], Nobuko Morisawa[1], Tsuneo Saga[3], Susumu Mori[4] & Kaori Togashi[1]

[1]Department of Diagnostic Imaging and Nuclear Medicine, Kyoto University, Kyoto, Japan, [2]Department of Radiology, University of Cambridge, Addenbrooke's Hospital, Cambridge, UK, [3]Molecular Imaging Center, National Institute of Radiological Sciences, Chiba, Japan and [4]Department of Radiology, Johns Hopkins University School of Medicine, Baltimore, MD, USA

Background: Diffusion tensor imaging (DTI) at 3 T provides information on the microstructure and pathophysiology of tissues that is not available from conventional imaging with an advantage of high signal to noise ratio (SNR).

Purpose: To evaluate the feasibility of DTI of the normal kidney at 3.0 T compared to results obtained at 1.5 T.

Material and Methods: DTI of the normal kidney of 15 healthy volunteers obtained with 3.0 and 1.5 T scanners using respiration-triggered acquisition was examined. Fractional anisotropy (FA) and apparent diffusion coefficient (ADC) values of both the renal cortex and the medulla and SNRs were measured (b-values 0 and 400 s/mm^2, diffusion direction of 6). The image quality of FA and ADC maps was also compared subjectively.

Results: The FA values of the renal cortex were 0.15 ± 0.03 at 3.0 T and 0.14 ± 0.03 at 1.5 T on average. This difference was not significant. The FA values of the renal medulla were 0.49 ± 0.04 at 3.0 T and 0.42 ± 0.05 at 1.5 T. ADC values of the renal cortex were 2.46 × 10^{-3} ± 0.09 mm^2/s at 3.0 T and 2.20 × 10^{-3} ± 0.11 mm^2/s at 1.5 T. The ADC values of the renal medulla were 2.08 × 10^{-3} ± 0.08 mm^2/s at 3.0 T and 1.90 × 10^{-3} ± 0.11 mm^2/s at 1.5 T. These FA and ADC values were consistent with previous publications. The difference was significant for the FA value of the medulla ($P < 0.01$) and ADC values in both cortex and medulla ($P < 0.01$). The subjective image quality of the FA map with the 3.0 T scanner was significantly superior to that with the 1.5 T scanner ($P < 0.01$), but not significant for the ADC map ($P = 0.18$). There was a significant difference in SNR between 3.0 T (48.8 ± 6.6) and 1.5 T images (32.8 ± 5.0).

Conclusion: The feasibility of renal DTI with a 3.0 T magnet resulting in improved SNR was demonstrated.

Key words: High-field MRI; fractional anisotropy; apparent diffusion coefficient

Aki Kido, MD, PhD, Department of Diagnostic Imaging and Nuclear Medicine, Kyoto University, 54 Kawahara-cho, Shogoin, Sakyo-ku, Kyoto 606-8507, Japan (tel. +81 75 751 3419, fax. +81 75 771 9709, e-mail. akikido@kuhp.kyoto-u.ac.jp

Submitted August 6, 2009; accepted for publication June 21, 2010

Diffusion-weighted MR images (DWI) allow quantitative measurement of water diffusion using apparent diffusion coefficient (ADC) values, which is a measure of diffusion constant of the tissue obtained from MR-DWI (1). In addition to water diffusion, we can also measure the anisotropy of water movement caused by the presence of axons, muscle fibers, or the vasculature using diffusion tensor MRI (DTI) (2–4). In short, DTI contains information of direction in addition to the amount of diffusion obtained from DWI. Fractional anisotropy (FA), a quantitative parameter of diffusion anisotropy, is commonly used to estimate diffusion anisotropy (5).

DTI can provide valuable information about the microstructure and pathophysiology of tissues that is not available from conventional imaging (6, 7). This technique is now applied to body organs, including the liver, heart, kidney, and prostate (8-11). Nonetheless, DTI of abdominal organs has proven to be challenging due to respiratory motion.

Recently, high-field 3.0 Tesla (T) MRI imaging has become more widely available for neurological imaging, and several studies with 3.0 T body MRI have reported favorable results (12–14). For body MRI, marked improvements in signal to noise ratio (SNR) have been

informa
healthcare

DOI 10.3109/02841851.2010.504741

demonstrated in several organs on T2-weighted and T1-weighted images (15, 16). However, the advantages of the high-field scanners may not always be clear for DTI. Image distortion due to B0 inhomogeneity can also be problematic. Accordingly, it is important to perform comparison studies for each organ to evaluate the advantages of a high-field scanner.

In this study, we examined the feasibility of DTI of the normal kidney at 3.0 T by comparing FA and ADC values obtained at 3.0 T with values obtained at 1.5 T using respiration-triggered acquisition.

Material and Methods

Study population

The ethics committee of our institute approved the protocol of this study. Written informed consent was obtained from all subjects.

The study population consisted of 16 healthy volunteers (age 22–41 years, mean 30.6 years; 12 men and 4 women). Exclusion criteria were previous renal disease, hypertension or other vascular diseases, and abnormal findings of the kidney on MRI. No specific pretreatments, such as fasting or drinking, were undertaken before the examination. In 4 years after this study, no one complained of or received treatment for renal dysfunction or disorders.

MR scanning protocol

MR images were obtained with a 3.0 T scanner (Trio; Siemens Medical Systems, Erlangen, Germany) and a 1.5 T scanner (Symphony, Siemens, Erlangen, Germany) using a phased-array body coil. The 3.0 T MR scanner was equipped with a 40 mT/m gradient (slew rate = 200 T/m/s), while the 1.5 T MR scanner was equipped with a 30 mT/m magnetic field gradient system (slew rate = 125 T/m/s). An eight-channel receiving array coil was used for the 3.0 T MR scanner and a six-channel receive array coil was used for the 1.5 T MR scanner. MR images were obtained sequentially in 9 of the 16 subjects. For the remaining seven subjects, imaging was performed on the same day. Axial and coronal half-Fourier acquisition single shot turbo spin echo (HASTE) scans were performed to localize the kidneys; then DWI was obtained using respiration-triggered acquisition (trigger delay 100 ms, respiratory phase expiratory) in a coronal plane. The optimum timing of trigger delay was determined in our pilot study and was kept fixed for all scans throughout the study (17). Respiratory triggering was monitored by the operator of the scan to ensure that acquisitions were adequately triggered. The following imaging parameters were used for both the 3.0 and 1.5 T scanners: TR, 2000 ms; TE, 74 ms; slice thickness, 3 mm; slice number, 5; b-values, 0 and 400 s/mm^2; diffusion directions, 6; number of signal averages, 3; base resolution, 128; pixel size, 2.5×2.5 mm; reduction factor for parallel imaging, 2; band width, 2056 Hz/pixel; field of view (FOV), 320 mm; and intersection gap, 1 mm. We used b-values of 400 s/mm^2 based on previous results (18). The above series of DWI were repeated four times to obtain sufficient signal. Because DWI was acquired by respiratory triggering, the acquisition time varied between the subjects, with mean acquisition time of 10.1 min (range 7.03–14.6 min). Coronal T2-weighted imaging was obtained as a screening to rule out morphological renal abnormalities.

Image analysis and statistical analysis

We selected the right kidney for analysis because of the relatively limited cardiac and respiratory motion artifact due to the presence of the liver above the right kidney. The qualitative evaluations of FA and ADC maps at both 3.0 T and 1.5 T scanner was done by two of the authors independently using blinded observers. When the result was different between readers, the score was discussed and determined with consensus. The evaluation score was as follows: 1, not evaluable; 2, poor (cortex-medulla differentiation is not visible); 3, moderate (fair) (cortex-medulla differentiation is visible but not clear); 4, good (reasonable cortex-medulla difference); 5, excellent (clear cortex-medulla difference). Due to non-normal distribution, the scores obtained from 3.0 T and 1.5 T were compared using Wilcoxon rank sum test.

For images with sufficient quality, the FA and ADC values of the renal cortex and medulla were measured using DtiStudio software, version 2.3 (19). The subjects for whom the image quality of FA or ADC map subjectively was evaluated as scale 1 (= not evaluable) were excluded from further evaluation of measuring the FA and ADC values and SNR. For region of interest (ROI) placement, one of five slices was selected that contained the maximum area of the right kidney and included as few renal vessels as possible to prevent flow-related artifacts. Two oval ROIs were placed over the renal cortex and medulla for both the upper and lower poles, as large as possible (Fig. 1). The same ROIs were used for both ADC and FA measurements. The mean ROI sizes for the renal cortex were 7.9 pixels for the 3.0 T scanner and 7.5 pixels for the 1.5 T scanner, while for the renal medulla the mean sizes were 11.0 and 10.5 pixels, respectively.

To measure the SNR of the kidney cortex, one ROI was placed on the right renal cortex on DWI. Cortex was used for SNR measurement to avoid artifacts from renal vessels. The SNR of renal cortex was defined as the signal intensity of the renal cortex divided by the standard deviation (SD) of the background noise.

Fig. 1. The oval ROIs were placed for evaluating FA and ADC values in renal cortex and medulla.

In this study, correction due to the usage of parallel imaging was not performed.

Due to non-normal distribution, statistical analyses were performed to evaluate the difference in ADC value and FA and SNR using Wilcoxon's rank sum test (SPSS 12.0J for Windows, Tokyo, Japan).

Results

Subjective image qualities of the FA at 3.0 T (4.2 ± 0.9) were superior to those at 1.5 T (score 4.2 ± 0.9 vs 3.1 ± 1.0; $P < 0.01$) (Fig. 2A and B). Regarding image quality of ADC maps, there was no significant difference between 3.0 T and 1.5 T (score 3.5 ± 1.2 vs 3.2 ± 0.9; $P = 0.18$) (Table 1). One subject was excluded from the analysis owing to non-evaluable image (FA and ADC map) quality, due to respiratory motion. Thus, 15 subjects were included in the further analysis.

The FA and ADC values of the renal cortex and medulla and SNR of the two scanners are shown in Table 2. The FA value of the renal cortex was 0.15 ± 0.03 at 3.0 T and 0.14 ± 0.03 at 1.5 T; this difference was not significant. The FA value of the renal medulla was significantly higher than that of the renal cortex at both 3.0 T (0.49 ± 0.04) and 1.5 T (0.42 ± 0.05) ($P < 0.01$). The ADC value of the renal cortex was 2.46 ± 0.09 × 0^{-3} mm^2/s at 3.0 T and 2.20 ± 0.11 ×10^{-3} mm^2/s at 1.5 T. The ADC value of the renal medulla was 2.08 ± 0.08 × 10^{-3} mm^2/s at 3.0 T and 1.90 ± 0.11 × 10^{-3} mm^2/s. This difference was significant in both cortex and medulla ($P < 0.01$).

The SNR of the kidney was 48.8 ± 6.6 in images at 3 T and 32.8 ± 5.0 in images at 1.5 T. There was a significant difference between them ($P < 0.01$).

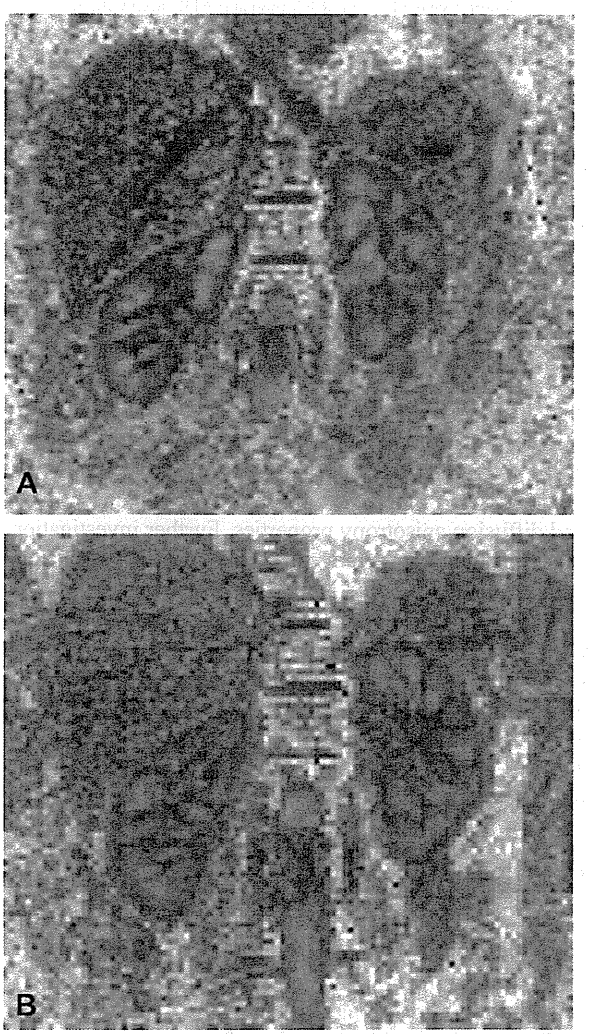

Fig. 2. (A) FA map obtained with a 3.0 T magnet. (B) FA map obtained with a 1.5 T magnet. The border and contrast between the renal cortex and medulla were more distinct in images obtained at 3.0 T than those obtained at 1.5 T.

Discussion

To the best of our knowledge, there are no reports evaluating the FA of the kidney on 3.0 T MRI using respiration-triggered acquisition. Our results show that the subjective image quality of FA maps at 3.0 T scanner is superior to that at 1.5 T. Superior subjective image quality of the FA map at 3.0 T is supposed to reflect higher SNR at 3.0 T to 1.5 T (13, 15, 20, 21). The slightly smaller amount of SD with 3.0 T than 1.5 T may also be explained by higher SNR at 3.0 T.

Our FA values for the renal medulla were larger than those for the renal cortex, similar to previous reports (11). It is thought that the renal medulla is more anisotropic due to the radial orientation of its structures (11). We found

Table 1. Qualitative evaluation of FA map and ADC map with 3.0 T and 1.5 T scanners.

Map	3 T	1.5 T	*P* value
FA	4.2 ± 0.9	3.1 ± 1.0	<0.01
ADC	3.5 ± 1.2	3.2 ± 0.9	0.42

Two readers independently scored both FA and ADC maps. When the result was different between readers, the score was discussed and determined with consensus. FA, fractional anisotropy; ADC, apparent diffusion coefficient. Evaluation score: 1, not evaluable; 2, poor (cortex-medulla differentiation is not visible); 3, moderate (fair) (cortex-medulla differentiation is visible but not clear); 4, good (reasonable cortex-medulla difference); 5, excellent (clear cortex-medulla difference). $P < 0.05$ was considered statistically significant.

a small but significant difference in FA and ADC values between the 1.5 and 3.0 T magnets. However, the cause of the difference is not clear. One possibility is that renal tissue consists of multiple compartments with different T2 and diffusion anisotropy properties. Further investigation is needed to elucidate the relation between FA values and renal anatomic structure.

One of the potential disadvantages of employing a high-field magnet for DTI is image distortion due to B0 susceptibility. In addition, ADC values for renal cortex and medulla obtained in our study were almost the same as those previously reported using 1.5 T magnets (11, 22). Therefore we may say that there is no clear advantage of using a 3.0 T magnet to obtain ADC maps.

We had a high success rate (15/16) for respiration triggering to perform kidney DTI in this study. Respiration-triggered acquisition is feasible with excellent cortex-medulla contrast for the kidney DTI image at 1.5 T (17). Respiration triggering reduces the burden on patients, in particular eliminating the need for long breath-holding. This allows us to use longer scanning times and to improve SNR. In the future, incorporation of navigator echoes that are widely used for cardiac imaging could further enhance the robustness to the elimination of motion (23, 24).

There are some limitations of this study. First, we included a limited number of subjects and none of the subjects had blood or urine analysis to evaluate renal function, although no subject had a prior history of renal disease or morphological abnormalities on MRI and no renal disease or dysfunction during 4 years after this study. Second, the ROIs of both the renal cortex and the medulla were very small (<8 pixels multiplied with 2.5 × 2.5 × 3 mm^3). Third, the spatial resolution of the DTI in our protocol might be insufficient to observe renal anatomy. Fourth, imaging was not acquired sequentially for all subjects, and was not performed in the same hydration status due to limited hardware availability. It has been reported that ADC values are not affected by hydration status (25). Although we did not examine the hydration effect in this study, the effect of water loading should be examined in various sequences including DTI. Finally, our study population did not include patients with renal diseases. Comparing the FA values of normal kidneys with those for patients with various renal diseases will be required to evaluate the clinical significance of renal FA values and the role of renal DTI.

Table 2. Quantitative evaluation of FA map and ADC map with 3.0 T and 1.5 T scanners.

	Parameter	1.5 T	3 T	*P* value
FA	Cortex	0.14 ± 0.03	0.15 ± 0.03	NS
	Medulla	0.42 ± 0.05	0.49 ± 0.04	<0.01
ADC ($\times 10^{-3}$)	Cortex	2.20 ± 0.11	2.46 ± 0.09	<0.01
	Medulla	1.90 ± 0.11	2.08 ± 0.08	<0.01
SNR		32.8 ± 5.0	48.8 ± 6.6	<0.01

FA, fractional anisotropy; ADC, apparent diffusion coefficient; SNR, signal to noise ratio.

So far, DWI has been used to evaluate renal dysfunction before kidney transplantation (26–28). A brain DTI-MRI study on multiple sclerosis reported that the abnormality undetected both on T2WI and DWI could be detected only by FA (29). The possibility of the detection of alteration in renal architecture due to various renal diseases has also been indicated even with breath-hold at 1.5T (30). Because the kidney consists of numerous tubular cells and because DTI can provide directional information in addition to DWI, DTI might allow the detection of renal dysfunction much earlier in people undergoing chemotherapy with a nephrotoxic agent, post-renal transplant, chronic renal disease such as interstitial fibrosis and tubular atrophy. As those conditions are difficult to detect by morphological change at MRI, such as T1- or T2-weighted imaging, the early detection of the renal dysfunction by DTI can be expected. In addition, the evaluation of perfusion is also needed to evaluate renal function. Intravoxel incoherent motion (IVIM) perfusion MRI can detect pure molecular diffusion and microcirculation or blood perfusion without using contrast agent (31, 32). Combining this technique with DTI, various renal functions that cannot be obtained by morphological information (perfusion, abnormality or change in renal dysfunction caused by drugs, etc.), will be evaluated without strain to the patients.

In conclusion, we demonstrated the feasibility of renal DTI with a 3.0 T magnet, resulting in improved SNR. FA and ADC values agreed with previous publications, but both sets of values were slightly higher for 3 T MRI than for 1.5 T MRI. Although our study is only a preliminary investigation, renal DTI obtained with a 3.0 T scanner can be used as a normative guide in addition to 1.5 T.

Acknowledgement

This study was supported by grand-in-aid no. 16209035 from the Ministry of Education, Culture, Sports, Science and Technology.

Declaration of interest: The authors report no conflicts of interest. The authors alone are responsible for the content and writing of the paper.

References

1. Le Bihan D, Turner R, MacFall JR. Effects of intravoxel incoherent motions (IVIM) in steady-state free precession (SSFP) imaging: application to molecular diffusion imaging. Magn Reson Med 1989;10:324–37.
2. Le Bihan D, Mangin JF, Poupon C, Clark CA, Pappata S, Molko N, et al. Diffusion tensor imaging: concepts and applications. J Magn Reson Imaging 2001;13:534–46.
3. Hsu EW, Muzikant AL, Matulevicius SA, Penland RC, Henriquez CS. Magnetic resonance myocardial fiber-orientation mapping with direct histological correlation. Am J Physiol 1998;274:H1627–34.
4. van Doorn A, Bovendeerd PH, Nicolay K, Drost MR, Janssen JD. Determination of muscle fibre orientation using Diffusion-Weighted MRI. Eur J Morphol 1996;34:5–10.
5. Basser PJ, Pierpaoli C. Microstructural and physiological features of tissues elucidated by quantitative-diffusion-tensor MRI. J Magn Reson B 1996;111:209–19.
6. Sinha S, Bastin ME, Whittle IR, Wardlaw JM. Diffusion tensor MR imaging of high-grade cerebral gliomas. Am J Neuroradiol 2002;23:520–7.
7. Ciccarelli O, Werring DJ, Barker GJ, Griffin CM, Wheeler-Kingshott CA, Miller DH, et al. A study of the mechanisms of normal-appearing white matter damage in multiple sclerosis using diffusion tensor imaging – evidence of Wallerian degeneration. J Neurol 2003;250:287–92.
8. Taouli B, Martin AJ, Qayyum A, Merriman RB, Vigneron D, Yeh BM, et al. Parallel imaging and diffusion tensor imaging for diffusion-weighted MRI of the liver: preliminary experience in healthy volunteers. Am J Roentgenol 2004;183:677–80.
9. Sinha S, Sinha U. In vivo diffusion tensor imaging of the human prostate. Magn Reson Med 2004;52:530–7.
10. Scollan DF, Holmes A, Winslow R, Forder J. Histological validation of myocardial microstructure obtained from diffusion tensor magnetic resonance imaging. Am J Physiol 1998;275:H2308–18.
11. Ries M, Jones RA, Basseau F, Moonen CT, Grenier N. Diffusion tensor MRI of the human kidney. J Magn Reson Imaging 2001;14:42–9.
12. Noeske R, Seifert F, Rhein KH, Rinneberg H. Human cardiac imaging at 3 T using phased array coils. Magn Reson Med 2000;44:978–82.
13. Masi JN, Sell CA, Phan C, Han E, Newitt D, Steinbach L, et al. Cartilage MR imaging at 3.0 versus that at 1.5 T: preliminary results in a porcine model. Radiology 2005;236:140–50.
14. de Bazelaire CM, Duhamel GD, Rofsky NM, Alsop DC. MR imaging relaxation times of abdominal and pelvic tissues measured in vivo at 3.0 T: preliminary results. Radiology 2004;230:652–9.
15. Edelman RR, Salanitri G, Brand R, Dunkle E, Ragin A, Li W, et al. Magnetic resonance imaging of the pancreas at 3.0 Tesla: qualitative and quantitative comparison with 1.5 Tesla. Invest Radiol 2006;41:175–80.
16. Kramer U, Nael K, Laub G, Nyborg GK, Fenchel M, Miller S, et al. High-resolution magnetic resonance angiography of the renal arteries using parallel imaging acquisition techniques at 3.0 T: initial experience. Invest Radiol 2006;41:125–32.
17. Kataoka M, Kido A, Yamamoto A, Nakamoto Y, Koyama T, Isoda H, et al. Diffusion tensor imaging of kidneys with respiratory triggering: optimization of parameters to demonstrate anisotropic structures on fraction anisotropy maps. J Magn Reson Imaging 2009;29:736–44.
18. Isoda H, Kataoka M, Maetani Y, Kido A, Umeoka S, Tamai K, et al. MRCP imaging at 3.0 T vs. 1.5 T: preliminary experience in healthy volunteers. J Magn Reson Imaging 2007;25:1000–6.
19. Jiang H, van Zijl PC, Kim J, Pearlson GD, Mori S. DtiStudio: resource program for diffusion tensor computation and fiber bundle tracking. Comput Methods Programs Biomed 2006;81:106–16.
20. Hinton DP, Wald LL, Pitts J, Schmitt F. Comparison of cardiac MRI on 1.5 and 3.0 Tesla clinical whole body systems. Invest Radiol 2003;38:436–42.
21. Chang KJ, Kamel IR, Macura KJ, Bluemke DA. 3.0-T MR imaging of the abdomen: comparison with 1.5 T. Radiographics 2008;28:1983–98.
22. Thoeny HC, De Keyzer F, Oyen RH, Peeters RR. Diffusion-weighted MR imaging of kidneys in healthy volunteers and patients with parenchymal diseases: initial experience. Radiology 2005;235:911–17.
23. Wang Y, Watts R, Mitchell I, Nguyen TD, Bezanson JW, Bergman GW, et al. Coronary MR angiography: selection of acquisition window of minimal cardiac motion with electrocardiography-triggered navigator cardiac motion prescanning – initial results. Radiology 2001;218:580–5.
24. Klessen C, Asbach P, Kroencke TJ, Fischer T, Warmuth C, Stemmer A, et al. Magnetic resonance imaging of the upper abdomen using a free-breathing T2-weighted turbo spin echo sequence with navigator triggered prospective acquisition correction. J Magn Reson Imaging 2005;21:576–82.
25. Damasio MB, Tagliafico A, Capaccio E, Cancelli C, Perrone N, Tomolillo C, et al. Diffusion-weighted MRI sequences (DW-MRI) of the kidney: normal findings, influence of hydration state and repeatability of results. Radiol Med 2008;113:214–24.
26. Namimoto T, Yamashita Y, Mitsuzaki K, Nakayama Y, Tang Y, Takahashi M. Measurement of the apparent diffusion coefficient in diffuse renal disease by diffusion-weighted echo-planar MR imaging. J Magn Reson Imaging 1999;9:832–7.
27. Vernathen P, Zumstein D, Einsenberg U, Simon-Zoula SC, Hofmann L, Boesch H, et al. Functional MRI of transplanted human kidneys evaluated by diffusion-weighted MRI – initial experience. In: 13th Annual Meeting of ISMRM. Miami, USA, 2005; abstract 556.
28. Thoeny HC, Zumstein D, Simon-Zoula S, Eisenberger U, De Keyzer F, Hofmann L, et al. Functional evaluation of transplanted kidneys with diffusion-weighted and BOLD MR imaging: initial experience. Radiology 2006;241:812–21.
29. Ciccarelli O, Werring DJ, Wheeler-Kingshott CA, Barker GJ, Parker GJ, Thompson AJ, et al. Investigation of MS normal-appearing brain using diffusion tensor MRI with clinical correlations. Neurology 2001;56:926–33.
30. Notohamiprodjo M, Glaser C, Herrmann KA, Dietrich O, Attenberger UI, Reiser MF, et al. Diffusion tensor imaging of the kidney with parallel imaging: initial clinical experience. Invest Radiol 2008;43:677–85.
31. Le Bihan D. Intravoxel incoherent motion perfusion MR imaging: a wake-up call. Radiology 2008;249:748–52.
32. Yamada I, Aung W, Himeno Y, Nakagawa T, Shibuya H. Diffusion coefficients in abdominal organs and hepatic lesions: evaluation with intravoxel incoherent motion echo-planar MR imaging. Radiology 1999;210:617–23.

Technical Note

Effect of Hyoscine Butylbromide (HBB) on the Uterine Corpus: Quantitative Assessment With T2-Weighted (T2W) MRI in Healthy Volunteers

Koji Fujimoto, MD,* Asako Nakai, MD, PhD, Tomohisa Okada, MD, PhD, Takashi Ikeuchi, MD, Naoe Satogami, MD, Sayaka Daido, MD, Masahiro Yakami, MD, and Kaori Togashi, MD, PhD

Purpose: To investigate effects of hyoscine butylbromide (HBB) on the appearance of three zonal anatomy of the uterine corpus on T2-weighted images (T2WI).

Materials and Methods: Sagittal T2WI of the pelvis were acquired before and after intramuscular administration of HBB with interval of 10 minutes in 22 healthy volunteers. By drawing polygonal regions of interest (ROIs), the uterine corpus was delineated into outer myometrium (OM), junctional zone (JZ), and endometrium (EM) in 20 subjects. Areas (mm^2) and relative signal intensity (rSI) of each layer were compared between pre-HBB and post-HBB administration images by using paired *t*-tests. Histogram analysis was conducted for the uterine layers and changes were visualized.

Results: Areas of OM were significantly increased ($P = 0.014$) and mean rSI of JZ and OM were significantly increased ($P = 0.007$ and 0.001, respectively) after administration of HBB. Histogram showed an increase in the number of pixels with higher rSI in the OM, which was considered to be caused by an increase in interstitial fluid and vascular dilatation. EM did not show significant changes.

Conclusion: Layer-wise ROI analyses demonstrated changes in the area and rSI in T2WI of the uterus after HBB administration. Histogram analysis contributed to the investigation of signal changes.

Key Words: hyoscine butylbromide; myometrium; uterus; T2-weighted imaging; female pelvis
J. Magn. Reson. Imaging 2010;32:441–445.

HYOSCINE N-BUTYLBROMIDE (HBB; Buscopan®, Boehringer Ingelheim, Ingelheim am Rhein, Germany) is used for the magnetic resonance imaging (MRI) of the female pelvis, because it suppresses contraction of smooth muscle in the intestine and reduces motion artifacts (1,2). Similar to the intestine, muscular layer of the uterus, or myometrium, consists of smooth muscle, and therefore the uterus is known to have contractility. Cine mode display of continuously obtained ultrafast MRI (cine-MRI) has enabled visualization of peristalsis of the uterus (3,4) and its variation with menstrual cycles (5), relationship with dysmenorrhea (6), intrauterine devices (7), oral contraceptives (OCs) (8), and endometriosis (9). Recently, by using this method, the effect of HBB to suppress uterine contractility was shown (10). The change of the uterine contractility may alter its size and signal intensity (SI) on the appearance of the uterus on fast spin-echo T2-weighted images (T2WI), although the literature is limited about the effects of HBB.

Due to these considerations, we hypothesized that administration of HBB suppresses uterine contractility and results in the increase in the extracellular (interstitial and vascular) water volume, leading to an increase in uterine size and SI on T2WI. Thus, we compared size and SI of the zonal structures of the uterine corpus on T2WI before and after administration of HBB and investigated feasibility of histogram analysis for visualizing the changes.

MATERIALS AND METHODS

This prospective study was approved by the local institutional review board and written informed consent was obtained from all subjects.

Study Population

A total of 22 healthy women of reproductive age (range = 22–31 years, mean = 26.8 years of age) were recruited for this study. Those who were using intrauterine contraceptive devices, known to have anatomic

Department of Diagnostic Imaging and Nuclear Medicine, Kyoto University Graduate School of Medicine, Kyoto, Japan.
*Address reprint requests to: K.F., Department of Diagnostic Imaging and Nuclear Medicine, Kyoto University Graduate School of Medicine, 54 Kawahara-cho, Shogoin, Sakyo-ku, Kyoto 606-8507, Japan. E-mail: kfb@kuhp.kyoto-u.ac.jp
Received September 18, 2009; Accepted April 29, 2010.
DOI 10.1002/jmri.22252
Published online in Wiley InterScience (www.interscience.wiley.com).

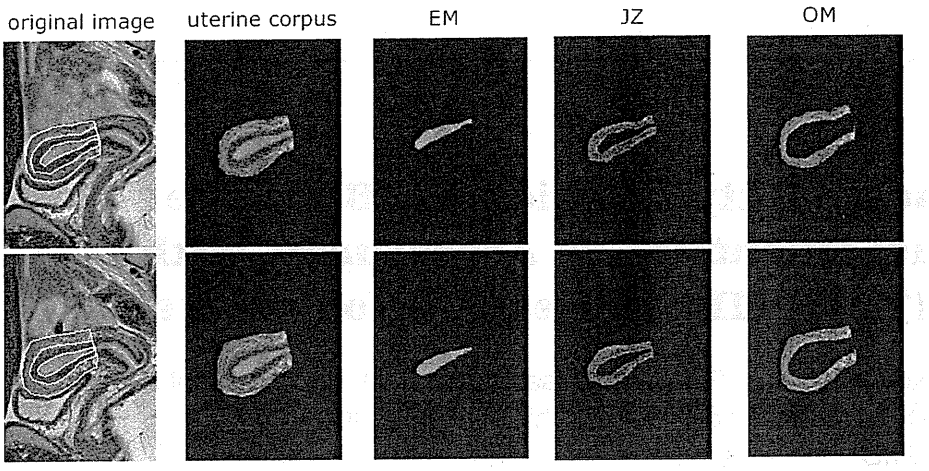

Figure 1. Sagittal T2WI of a 28 years-old female before (upper row) and after (lower row) administration of hyoscine butylbromide. Outer contours of the uterine corpus, junctional zone (JZ), and the endometrium (EM) were delineated by drawing polygonal ROIs. By using an in-house software created on MATLAB, three zonal layers of EM, JZ and outer myometrium (OM) were separately shown. Window levels and window widths were identical for all images.

uterine anomalies, history of cardiac diseases, or glaucoma were excluded. Those who were taking OCs were also excluded since the drugs were reported to suppress uterine peristalsis (8). The phase of the menstrual cycle was not considered in this study.

Image Acquisition

MR images were obtained using a 3.0 T scanner (Trio; Siemens Medical Systems, Erlagen, Germany) or a 1.5 T scanner (EXCELART Vantage, powered by Atlas; Toshiba Medical Systems, Otawara, Japan) with a multi-channel phased array coil. After obtaining three-plane localizing images, axial T2WI were obtained, followed by sagittal T2WI parallel to the long axis of the uterine corpus. For the 3.0 T scanner, parameters for sagittal T2WI were: TR/TE = 4800/107 msec; matrix size = 336 × 448; field-of-view = 195 × 260 mm^2. Nominal voxel size resulted in 0.59 × 0.59 × 3 mm^2 with 0.9 mm inter-slice gap. For the 1.5 T scanner, parameters for sagittal T2WI were: TR/TE = 4000/80 msec; matrix size = 384 × 512; field-of-view = 195 × 260 mm^2. Nominal voxel size resulted in 0.51 × 0.51 × 5 mm^2 with 1.5 mm inter-slice gap. After obtaining these images, 20 mg of HBB was administrated intramuscularly and sagittal T2WI were again obtained with identical parameters after 10 minutes. For imaging at the 3.0 T scanner, a dielectric pad was placed on the lower abdomen of the subject in order to reduce RF field inhomogeneity effect. In order to minimize the effect of the bladder filling, all volunteers were asked to empty the bladder before scanning.

Image Analysis

Shift of the uterine corpus between pre-HBB and post-HBB administration was visually evaluated, and one case that showed large through-plane shift was excluded from further analysis, for whom the uterus was not imaged in the midsagittal plane in the post-HBB scan. In another subject, the border between the outer myometrium (OM) and the junctional zone (JZ) could not be determined because of the myometrial contraction in pre-HBB administration images and this case was also excluded. For the remaining 20 cases, polygonal regions of interest (ROIs) were drawn to delineate contour of the uterine corpus, JZ and endometrium (EM) on a midsagittal image of the uterine corpus (Fig. 1). The uterine corpus was defined as uterine tissue above the level of the internal orifice of the uterus (6) and the borderlines between EM & JZ and JZ & OM were drawn where contrasts between two layers were largest.

ROI analysis of the uterus was performed for only one midsagittal image in each scans, since determination of the borders of each uterine layer, especially for those between OM and JZ, was difficult in many cases for images other than the midsagittal image due to the partial volume effect. ROI drawings were performed with careful attention to minimize the effect of the uterine position change due to the bladder filling.

Reference ROIs were drawn on the paraspinal muscles and subcutaneous fat in the hip, avoiding vessels and ghosting artifacts. These ROIs placed on the pre-HBB administration images were copied and pasted to post-images in order to minimize effect of the displacement with modification to avoid aforementioned structures.

In order to minimize differences in SI between different acquisitions and different MR scanners, SI of each ROI was converted to the relative SI (rSI) by the following formula:

$$\text{relative SI} = (\text{mean SI of each uterine region} - \text{mean SI of paraspinal muscle})/(\text{mean SI of fat} - \text{mean SI of paraspinal muscle}) \times 100$$

As a consequence, rSI of 0 and 100 corresponded to rSI of paraspinal muscle and fat, respectively. Areas (mm^2) of the three zonal layers of the uterine corpus were calculated by:

$$\text{Areas}(mm^2) = \text{numbers of pixels in each uterine layers} \times \text{voxel size}$$

In order to visualize distribution and changes of rSI in each uterine layer and the entire myometrium (i.e., OM + JZ), histograms were drawn for each subjects

Table 1
The Areas and Relative Signal Intensity (rSI) in Pre- and Post-Administration of Hyoscine Butylbromide†

	Area (mm^2)				rSI			
	EM	JZ	OM	Myometrium (JZ + OM)	EM	JZ	OM	Myometrium (JZ + OM)
Pre	174 ± 128	556 ± 155	976 ± 325	1533 ± 355	74.6 ± 16.9	24.1 ± 9.1	38.5 ± 10.5	33.0 ± 9.9
Post	174 ± 120	542 ± 171	1065 ± 315	1606 ± 377	76.7 ± 17.0	26.1 ± 10.4	42.3 ± 12.8	36.5 ± 12.0
P values	0.822	0.576	0.014*	0.011*	0.307	0.007*	0.001*	0.001*

†Results were shown in means ± standard deviations (SD). Relative signal intensity was calculated by using signal intensities of the paraspinal muscle and the subcutaneous fat.
**P* values less than .05 were considered to indicate presence of significant difference. EM = uterine endometrium, JZ = junctional zone, OM = outer myometrium.

by plotting fraction of pixels per total pixels of the uterine corpus against rSI for pre-HBB and post-HBB administration scans and subtracted histograms were overlaid. Histograms were then, averaged for all subjects. To reduce the effect of random noise, images were smoothed by using a Gaussian filter before histogram analyses. These image processing were performed by using an in-house software developed on MATLAB R2008a (Mathworks Inc., Natick, MA, USA).

Statistical Analysis

First, in order to evaluate stability of reference SI before and after HBB administration, reference SI of each subject was calibrated for each tissue type (i.e., muscle or fat) by dividing by the average SI of all of the subjects separately for each scanner. Then, calibrated reference SI for pre-HBB and post-HBB administration scans were compared as a whole. Second, areas (mm^2) and mean rSI of the EM, JZ, OM, and the entire myometrium (i.e., JZ + OM) were compared between pre-HBB and post-HBB administration scans. The percentage of the JZ against the entire myometrium was also calculated and compared. Comparisons of the results were performed by using paired *t*-tests, and *P*-values less than 0.05 were considered to indicate statistically significant differences.

RESULTS

Incidental uterine leiomyoma or adenomyosis were not found in any of the cases.

No significant difference was observed in calibrated SI of the reference ROIs at the paraspinal muscle ($P = 0.42$) and the subcutaneous fat ($P = 0.94$) between pre-HBB and post-HBB administration scans. Means and standard deviations (SDs) of areas and rSI of the uterine EM, JZ, OM, and the entire myometrium of all subjects and their *P* values of the paired *t*-tests were summarized in Table 1. Mean increases in rSI were 2.8, 8.4, 9.9, and 10.6 (%), and mean changes in the area were −0.9, −2.0, 7.5, and 4.0 (%) respectively for the EM, JZ, OM, and the entire myometrium. The mean rSI of the JZ, OM, and the entire myometrium were significantly higher and the mean areas of the OM and the entire myometrium were significantly larger in post-HBB administration scans than in pre-HBB scans. The mean area of the JZ was slightly decreased after HBB administration but the difference was not significant ($P = 0.576$). The percentage of the JZ against the entire myometrium was 38.3 and 35.6 (%), respectively for pre-HBB and post-HBB scans and the difference was not statistically significant ($P = 0.059$). Areas and rSI of the EM did not show significant differences ($P = 0.822$ and 0.307, respectively).

On histograms averaged for all subjects, plots of pre-HBB and post-HBB administration scans showed similar shapes with a slight shift toward higher rSI distribution in the JZ, OM and the entire myometrium (Fig. 2).

DISCUSSION

HBB suppresses intestinal peristalsis by blocking the acetylcholine receptor of the parasympathetic system. Similar to the intestine, uterine myometrium is composed of smooth muscle, which has the ability to contract, and therefore uterine contraction would be suppressed by HBB. According to a previous study using "cine-MRI", decreased frequency of uterine peristalsis was observed after administration of HBB, whereas intestinal peristalsis was suppressed more effectively (10). The authors discussed that this difference may be due to the effect of residual adrenergic mechanisms between the intestine and the uterus. Adrenergic mechanisms simply suppress intestinal muscle contractions through adrenergic alpha-2 receptors (11), whereas there are two opposing effects on uterine myometrial contractility, i.e., stimulation through alpha-1 receptors and suppression through beta-2 receptors (11). In addition, other mechanisms including myogenic or hormonal pathways might have additional effects. The authors also implied that suppression of uterine myometrial contractility might improve quality of T2WI, although it was not examined in detail. Results of our study may suggest that the effect of HBB could be observed as an increase in the area and rSI on T2WI, and that this effect was observed even in the myometrium that does not show apparent contraction.

An increase in areas and rSI of the entire myometrium on T2WI is considered to reflect an increase in water or blood content in this area. It may be caused by increased fluid in extracellular space as well as an increase in vascular space within the myometrium. Another possibility is cell swelling caused by an increase in intracellular fluid, but this is not likely the case because the amount of the water inside the cell

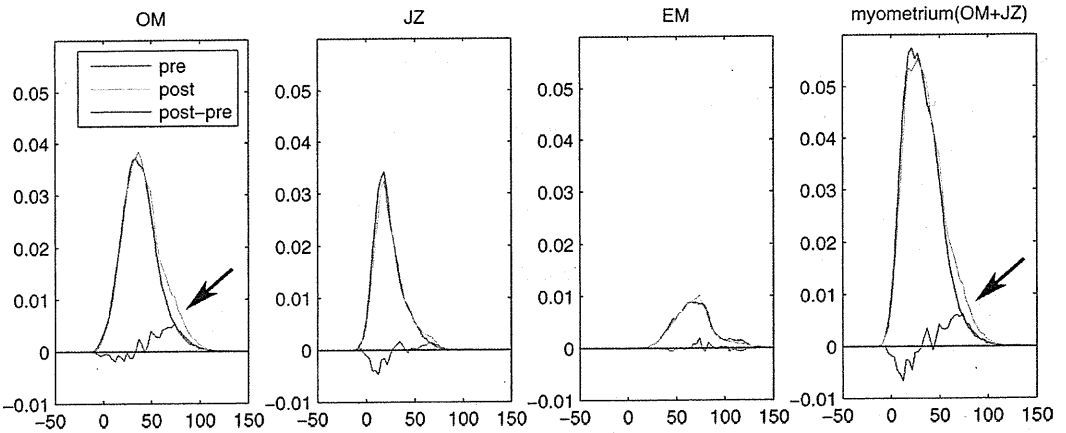

Figure 2. Averaged histograms of all subjects for relative signal intensity (rSI) of three zonal layers and the entire myometrium (OM + JZ) of the uterus are presented for pre (red lines) and post (green lines) administration of hyoscine butylbromide (HBB). Their differences are plotted in blue lines. Horizontal axis indicates rSI and vertical axis indicates fraction of pixel counts per total pixels of the uterine corpus. Note the similarity of histograms with slight shift to higher rSI after HBB administration in the OM, JZ and whole myometrium. Also note the difference in right slopes of the histograms in the OM and the entire myometrium (arrows). Relative SI of 0 and 100 correspond to rSI of paraspinal muscle and subcutaneous fat, respectively. EM: endometrium, JZ: junctional zone and OM: outer myometrium.

is relatively preserved (12). Results of histogram analyses also seem to support this interpretation. Averaged histogram plots of pre-HBB and post-HBB administration showed similar shapes with a small amount of shift toward higher rSI values in the JZ and OM, as well as in the entire myometrium. In addition, for OM and the entire myometrium, right slopes of their histograms were slightly wider after HBB-administration (Fig. 2). Shift of the histograms toward higher rSI may reflect global increase in rSI in the myometrium, whereas changes in the right slopes of the histograms may partially reflect regional increase in rSI, such as vessel dilatation. However, limitation in spatial resolution makes it difficult to discriminate vascular structure from interstitial fluid. Subtraction of images between pre-HBB and post-HBB administration scans might show the difference, but it was not possible because the size, shape, and location of the uterus were not identical between two scans. For discriminating vascular structure from interstitial fluid, perfusion MRI might be helpful, with which physiologic changes and correlation between perfusion and T2 (transverse relaxation time) of the uterine myometrium were shown (13).

Role of the myometrial contraction for blood circulation was discussed in previous studies (14,15), where "squeezing out" of blood and/or interstitial fluid in the uterine myometrium was considered to be important. A short time interval of 10 minutes between two scans before and after administration may favor for an increase in the vascular space (i.e., vascular dilatation) rather than in the interstitial fluid, although it cannot be concluded from this study. Similar to the current result, relatively bright and swollen uteri on T2WI were observed in recipients of OCs (16). In those cases, possible causes were considered to be myometrial edema together with vasodilatation secondary to hormonal change (17).

Mean area of the JZ was not significantly different after HBB administration. In this study, we delineated the JZ as the inner layer of the myometrium that exhibited low SI. Previous investigations have explained that the higher SI of the OM compared to the JZ results from richer water content in the interstitium, increased extracellular matrix, and less tightly packed muscle cells (18,19). Nevertheless, the "JZ" in pathologic specimens is not completely concordant with those that appear in MR images. Since the authors defined the area of the JZ visually and respectively for each image, the border between the JZ and OM was not identical between pre-HBB and post-HBB scans. HBB might increase water content in the JZ and hence outer part of the JZ in pre-HBB scans might be classified as a part of the OM in post-HBB images, resulting in the shift of the borderline between JZ and OM toward inside. However, this mismatch of ROIs between two scan conditions does not impair our observations, because the myometrium as a whole (i.e., JZ + OM) still shows significant increase in its area and rSI.

Mean increase in rSI for the entire myometrium was 10.6 % and was larger than those of JZ and OM (8.4 and 9.9 %, respectively). The reason that the change in the entire myometrium was larger when results of two zonal structures (i.e., JZ and OM) were combined is explained by the changes in the proportion of each zonal structure between pre-HBB and post-HBB scans.

There are several limitations in this study. First, we did not consider the phase of the menstrual cycle. Previous reports have shown that strong myometrial contraction is seen at menstrual phase, whereas uterine peristalsis is observed most frequently during a periovulatory phase (20). Since phases of the menstrual cycle were not considered in this study, it is unclear whether HBB affects similarly between different phases. Second, age of the subjects were relatively younger, therefore we could not discuss the results regarding the different age populations. Lastly, some effects of the contraction and motion were unavoidable,

because uterine contraction and peristalsis were not completely suppressed even after administration of HBB (10).

In conclusion, this study showed that the size of the OM and the rSI of the OM and the JZ were significantly increased by administration of HBB. Layer-wise analysis in combination with histograms was feasible and contributed to the evaluation of changes in the area and rSI of the uterine myometrium.

ACKNOWLEDGMENTS

We thank Chiaki Imura, Kanae Yamamoto and Yoshiaki Komori (Siemens-Asahi Medical Technologies Ltd., Japan) for their technical advice and helpful discussions; Dr. Aki Kido (Department of Diagnostic Imaging and Nuclear Medicine, Kyoto University) for her professional advice.

REFERENCES

1. Dosda R, Marti-Bonmati L, Ronchera-Oms CL, Molla E, Arana E. Effect of subcutaneous butylscopolamine administration in the reduction of peristaltic artifacts in 1.5-T MR fast abdominal examinations. Eur Radiol 2003;13:294–298.
2. Winkler ML, Hricak H. Pelvis imaging with MR: technique for improvement. Radiology 1986;158:848–849.
3. Masui T, Katayama M, Kobayashi S, et al. Changes in myometrial and junctional zone thickness and signal intensity: demonstration with kinematic T2-weighted MR imaging. Radiology 2001; 221:75–85.
4. Fujiwara T, Togashi K, Yamaoka T, et al. Kinematics of the uterus: cine mode MR imaging. Radiographics 2004;24:e19.
5. Nakai A, Togashi K, Yamaoka T, et al. Uterine peristalsis shown on cine MR imaging using ultrafast sequence. J Magn Reson Imaging 2003;18:726–733.
6. Kataoka M, Togashi K, Kido A, et al. Dysmenorrhea: evaluation with cine-mode-display MR imaging--initial experience. Radiology 2005;235:124–131.
7. –Kido A, Togashi K, Kataoka ML, Nakai A, Koyama T, Fujii S. Intrauterine devices and uterine peristalsis: evaluation with MRI. Magn Reson Imaging 2008;26:54–58.
8. Kido A, Togashi K, Nakai A, Kataoka ML, Koyama T, Fujii S. Oral contraceptives and uterine peristalsis: evaluation with MRI. J Magn Reson Imaging 2005;22:265–270.
9. Kido A, Togashi K, Nishino M, et al. Cine MR imaging of uterine peristalsis in patients with endometriosis. Eur Radiol 2007;17: 1813–1819.
10. Nakai A, Togashi K, Kosaka K, et al. Do anticholinergic agents suppress uterine peristalsis and sporadic myometrial contractions at cine MR imaging? Radiology 2008;246:489–496.
11. Moss J, Renz C. The autonomic nervous system. In: Miller RD, editor. Anesthesia 5th edition. Churchill Livingstone: Philadelphia, USA; 2000. p 523–577.
12. Ho SN. Intracellular water homeostasis and the mammalian cellular osmotic stress response. J Cell Physiol 2006;206:9–15.
13. Hoad CL, Fulford J, Raine-Fenning NJ, Campbell BK, Johnson IR, Gowland PA. In vivo perfusion, T1, and T2 measurements in the female pelvis during the normal menstrual cycle: a feasibility study. J Magn Reson Imaging 2006;24:1350–1356.
14. Danforth DN, Ueland K. Physiology of uterine action. In: Danforth DN, Scott J R, editors. Obstetrics and gynecology. 5th edition. Philadelphia, PA: Lippincott; 1986. p 582–628.
15. Sarnpson JA. The influence of myomata on the blood supply of the uterus, with special reference to abnormal uterine bleeding. Surg Gynecol Obstet 1913;16:144–180.
16. McCarthy S, Tauber C, Gore J. Female pelvic anatomy: MR assessment of variations during the menstrual cycle and with use of oral contraceptives. Radiology 1986;160:119–123.
17. Bartoli JM, Moulin G, Delannoy L, Chagnaud C, Kasbarian M. The normal uterus on magnetic resonance imaging and variations associated with the hormonal state. Surg Radiol Anat 1991; 13:213–220.
18. Brown HK, Stoll BS, Nicosia SV, et al. Uterine junctional zone: correlation between histologic findings and MR imaging. Radiology 1991;179:409–413.
19. Scoutt LM, Flynn SD, Luthringer DJ, McCauley TR, McCarthy SM. Junctional zone of the uterus: correlation of MR imaging and histologic examination of hysterectomy specimens. Radiology 1991;179:403–407.
20. Lyons EA, Taylor PJ, Zheng XH, Ballard G, Levi CS, Kredentser JV. Characterization of subendometrial myometrial contractions throughout the menstrual cycle in normal fertile women. Fertil Steril 1991;55:771–774.

10.1109/ULTSYM.2009.0594

Small Calculus Detection for Medical Acoustic Imaging Using Cross-Correlation between Echo Signals

Hirofumi Taki, Takuya Sakamoto, Toru Sato
Graduate School of Informatics
Kyoto University
Kyoto, Japan
hirofumi.taki@mb6.seikyou.ne.jp

Makoto Yamakawa
Advanced Biomedical
Engineering Research Unit
Kyoto University
Kyoto, Japan

Tsuyoshi Shiina
Graduate School of Medicine
Kyoto University
Kyoto, Japan

Abstract—**Small calculus detection is important to differentiate malignant from benign masses. Although ultrasonography has an excellent ability to depict soft tissue, it plays a secondary role in detection because of its poor calculus sensitivity compared with computed tomography and other X-ray tests. In this paper, we propose a novel method to detect small calculi using cross-correlation coefficients between IQ data of adjacent scan lines. Results of an experimental study show that the proposed calculus detection method has the potential to depict small calculi about 0.3 mm in diameter.**

Keywords-Ultrasonography; calculus; correlation; CT; CFAR

I. INTRODUCTION

Ultrasonography (US) has an excellent ability to depict soft tissue without ionizing radiation [1, 2], and thus has been used widely on clinical placement. However, the detectability of US for small calculi is insufficient compared with computed tomography (CT) and other X-ray tests. As a result, US often plays a secondary role when making distinctions between malignant and benign masses. Therefore the improvement of US in calculus detection is strongly desired to serve a convenient and effective imaging tool.

The echo scattered from a calculus has high intensity, and thus one strategy to detect calculi is to extract regions with high echo intensity in a B-mode image. This problem is equivalent to detecting targets in unstable noise and clutter while maintaining a constant probability of false alarm. To solve this problem, Finn et al. and Hansen et al. designed cell averaging constant false alarm rate (CA CFAR) detectors to set a threshold adaptively according to local noise levels [3, 4]. CA CFAR detectors have been employed for target detection in inhomogeneous medium [5, 6]. However, the echo intensity scattered from a small calculus is weak compared with that of a specular echo, indicating that this strategy is not suitable for small calculus detection.

Tissue harmonic imaging (THI) improves contrast resolution of US by suppression of speckle artifacts [7, 8]. The calculus detectability of THI is higher than that of conventional US; however, THI has a considerably low sensitivity compared with CT and other X-ray tests. By contrast, spatial compound imaging constructs a single B-mode image from multiple sweeps [9, 10]. This technique suppresses acoustic shadowing, one of the essential components to detect calculi. Therefore, spatial compound imaging is inappropriate for calculus detection.

In this study, we propose a novel calculus detection method using correlation coefficients between IQ data of adjacent scan lines, and experimentally verified the potential of the proposed method to detect small calculi about 0.3 mm in diameter.

II. METHODS

The proposed calculus detection method employs the cross-correlation coefficients between raw ultrasound in-phase and quadrature (IQ) data of adjacent scan lines behind a measurement point. When a calculus exists in a transmit beam, the waveform of a transmit pulse changes considerably. Therefore, the echo waveform of a scan line with a calculus is quite different from that without a calculus, where the echoes return from a range behind the calculus. Fig. 1 shows the schema of this process. We can presume the existence of a calculus from a decrease in cross-correlation coefficients. The correlation coefficient behind a measurement point with a Wiener filter is expressed as follows:

$$G(x,z,l)=\frac{\left|\sum_{z'=z_1}^{z_2} g(x,z')g(x+\Delta X,z'+l\Delta Z)^*\right|}{\sqrt{\sum_{z'=z_1}^{z_2}\left|g(x,z')\right|^2\sum_{z'=z_1}^{z_2}\left|g(x+\Delta X,z'+l\Delta Z)\right|^2}}, \quad (1)$$

where x and z are the lateral and vertical components, respectively, of a measurement point on a B-mode image, $g(x,z)$ is the IQ datum at P(x,z), a pixel in a B-mode image, $g(x,z)^*$ is the conjugate of $g(x,z)$, ΔX is the interval of scan lines, ΔZ is the range interval, z_1 and z_2 are the minimum and maximum of the z coordinates of a correlation window behind P(x,z).

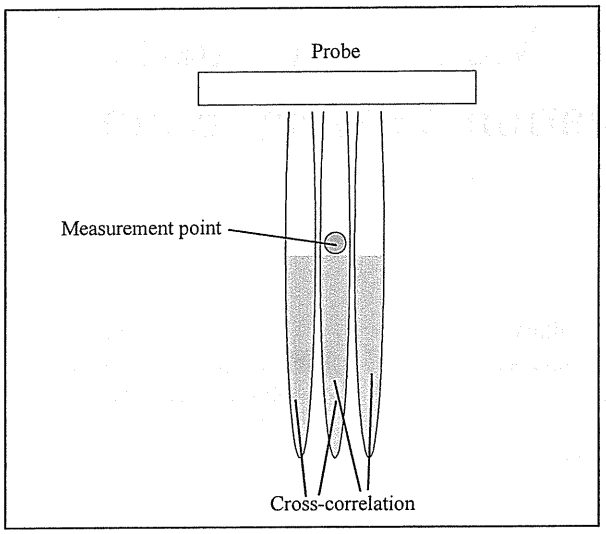

Figure 1. Cross-correlation between IQ data of adjacent scan lines.

A correlation coefficient is suppressed by not only a calculus, but also noise. When signals cut out by correlation windows have low signal-to-noise ratio (SNR), the effect of noise on the correlation coefficients is emphasized, interfering with the detection of the decrease on correlation coefficients originated by a calculus. In this study, we employed a modified Wiener filter to suppress the influence of noise on cross-correlation coefficients calculated by the proposed method. The cross-correlation coefficient with a modified Wiener filter is expressed as follows:

$$r\left(x+\frac{\Delta X}{2},z\right)=\frac{\left|\sum_{z'=z_1}^{z_2} g(x,z')g(x+\Delta X,z'+L\Delta Z)^*\right|+N}{\sqrt{\sum_{z'=z_1}^{z_2}|g(x,z')|^2\sum_{z'=z_1}^{z_2}|g(x+\Delta X,z'+L\Delta Z)|^2}+N}, \quad (2)$$

$$N=\alpha I_t, \quad (3)$$

Where N is a constant to raise a cross-correlation coefficient to 1 when the echo intensity cut out by a correlation window is low, α is a real number and I_t is the signal intensity at 0.5% from the maximum. L is equal to l when the correlation coefficient behind a measurement point, $G(x, z, l)$, is maximum.

III. Calculus Phantom Setup

A. Calculus Phantom

When a layered structure exists just behind a calculus, specular echoes scattered from the layered structure interfere with the detection of the calculus. To investigate the effect of the proposed calculus detection method in a severe condition mentioned above, we prepared a calculus phantom with a layered structure, as shown in Fig. 2. Three copper wires 0.2, 0.29 and 0.4 mm in diameter were embedded in an agar gel block at 2 cm depth at 1 cm intervals. A polyethylene sheet 0.1 mm thick was positioned closely behind the wires. The Agar gel contained 0.5% spherical polymer particles 7 μm in diameter (Tech Polymer; Sekisui Plastics Co., LTD.).

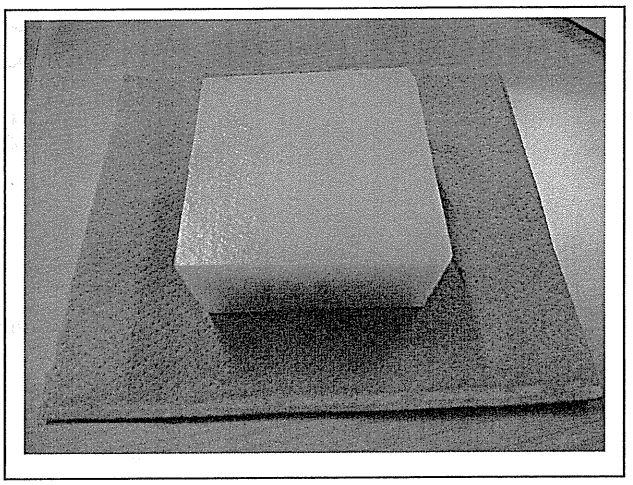

Figure 2. .Calculus phantom utilized in this study.

B. Acoustic Imager

We utilized IQ data exported from a commercial medical acoustic imager (EUB-8500; Hitachi Co. LTD.). US was performed with a linear array probe, where the scan line interval was about 0.13 mm and the center frequency of a transmit pulse was 7.5 MHz.

IV. Results

A. Calculation of N

Figure 3 shows the intensity distribution of a B-mode image. We assumed that the average noise intensity of an IQ datum of a pixel is I_t when noise intensity is maximum in a signal cut out by a correlation window. To raise the correlation coefficient to 0.8 in the case that SNR is 0 and average noise intensity is I_t, we set N as $4HI_t$, where H is the number of pixels in a signal cut out by a correlation window.

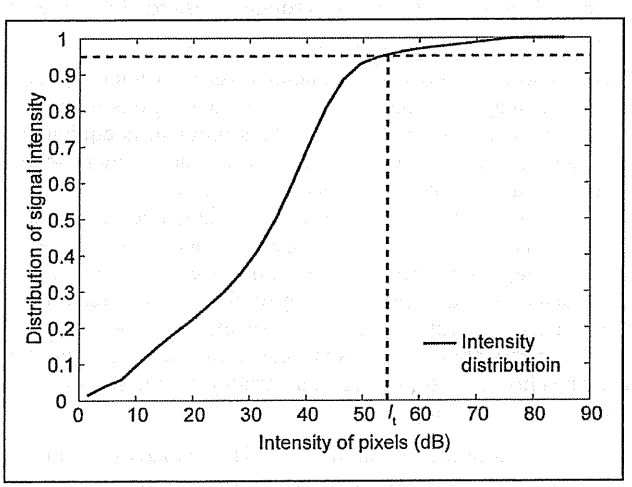

Figure 3. Intensity distribution of a B-mode image. The broken line shows the intensity at 0.5% from the maximum.

B. *Detection of Small Calculi Using Correlation Coefficients*

Figure 4 shows a B-mode image of a calculus phantom. A specular echo returned from a polyethylene sheet just behind calculi. The echoes scattered at three calculi are not outstanding in echo intensity as compared with the specular echo. This indicates that CFAR is not suitable for small calculus detection.

We first calculated cross-correlation coefficients between IQ data of adjacent scan lines, as shown in Fig. 5. When the constant N in (1) is equal to 0, i.e. using a Wiener filter, dips in the correlation coefficients appeared around the calculus positions in the profile and extended along the range direction to the length of correlation window. However, several dips also existed at various positions. In addition, correlation coefficients are notably low in the cases where correlation windows do not contain a layered structure.

It is expected that the low correlation coefficients originated from a lack of sufficient SNR. To suppress the decrease of correlation coefficients caused by noise effects in low SNR cases, we calculated correlation coefficients using a modified Wiener filter, where the constant N is equal to $4HI_t$. When correlation windows do not contain a layered structure and signal SNR cut out by the window are expected to be low, correlation coefficients are raised to ≥ 0.8, as shown in Fig. 6. This verified the validity of the assumption about the average noise intensity above. The modified Wiener filter also forces most dips to be inconspicuous. By contrast, three dips of correlation coefficients remained at the wire positions. These results indicate that the waveform change of transmit pulses originating from a calculus can be detected by cross-correlation between IQ data of adjacent scan lines.

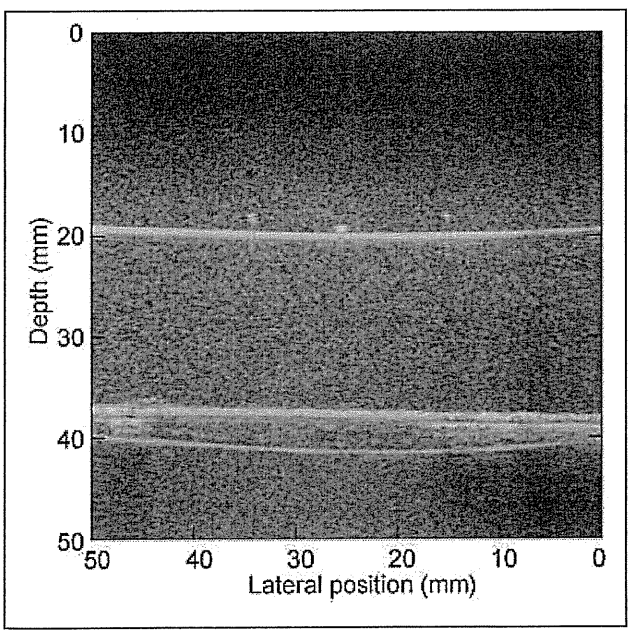

Figure 4. B-mode image of a calculus phantom.

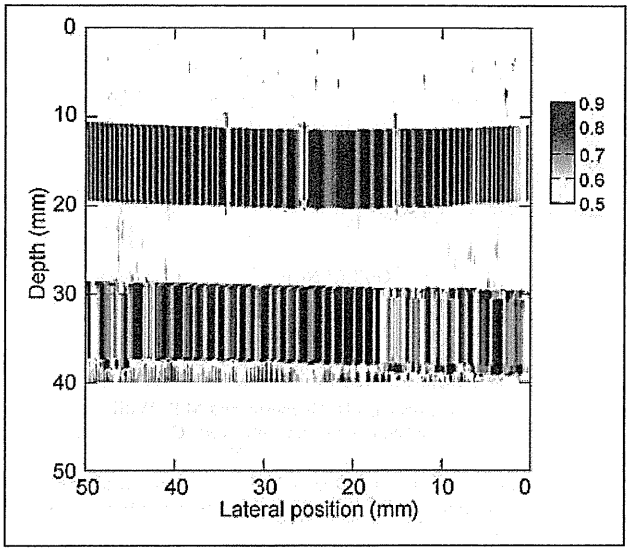

Figure 5. Correlation coefficients between IQ data of adjacent scan lines. where the constant N in (1) is equal to 0..

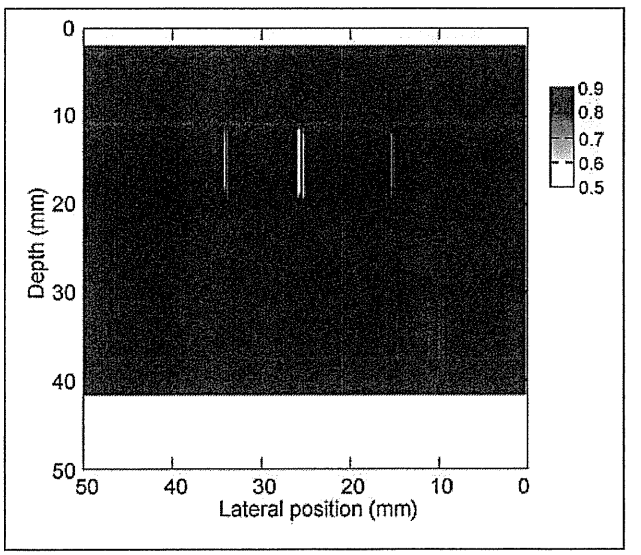

Figure 6. Correlation coefficients between IQ data of adjacent scan lines. where the constant N in (1) is equal to $4HI_t$..

V. Conclusions

We proposed a novel calculus detection method using correlation coefficients between IQ data of adjacent scan lines with a modified Wiener filter. To improve the specificity of the proposed method, we determined a proper constant to raise correlation coefficients in low SNR cases. An experimental study shows the ability of the proposed method for the detection of small calculi about 0.3 mm in diameter. This result suggests that the proposed calculus detection method has the potential to improve US tests in calculus detection.

ACKNOWLEDGMENTS

This work is partly supported by the Research and Development Committee Grants of the Japan Society of Ultrasonics in Medicine, Japan and the Innovative Techno-Hub for Integrated Medical Bio-imaging Project of the Special Coordination Funds for Promoting Science and Technology, from the Ministry of Education, Culture, Sports, Science and Technology (MEXT), Japan.

REFERENCES

[1] H. Özdemir, M.K. Demir, O. Temizöz, H. Genchellac, and E. Unlu, "Phase inversion harmonic imaging improves assessment of renal calculi: a comparison with fundamental gray-scale sonography," J. Clin. Ultrasound., vol. 36, pp.16-19, 2008.

[2] K.A.B. Fowler, J.A. Locken, J.H. Duchesne and M.R. Williamson, "US for detecting renal calculi with nonenhanced CT as a reference standard," Radiology, vol. 222, pp.109-113, 2002.

[3] H.M. Finn and R.S. Johnson, "Adaptive detection mode with threshold control as a function of spatially sampled clutter-level estimates," RCA Rev., vol.29, pp.414-465, 1968.

[4] V.G. Hansen and H.R. Ward, "Detection performance of the cell averaging LOG/CFAR receiver," IEEE Trans. Aerosp. Electron. Syst., vol. 5, pp.648-652, 1972.

[5] Y. Zhu and J.P. Weight, "Ultrasonic nondestructive evaluation of highly scattering materials using adaptive filtering and detection," IEEE Trans. Ultrason. Ferroelect. Freq. Contr., vol. 41, pp.26-33, 1994.

[6] N. Kamiyama, Y. Okamura, A. Kakee and H. Hashimoto, "Investigation of ultrasound image processing to improve perceptibility of microcalcifications," J Med. Ultrasonics., vol. 35, pp.97-105, 2008.

[7] T. Schmidt, C. Hohl, P. Haage, M. Blaum, D. Honnef, C. Weiß, G. Staatz and R. W. Günther, "Diagnostic accuracy of phase-inversion tissue harmonic imaging versus fundamental B-mode sonography in the evaluation of focal lesions of the kidney," AJR Am. J. Roentgenol., vol. 180, pp.1639-1647, 2003.

[8] E.L. Rosen and M.S. Soo, "Tissue harmonic imaging sonography of breast lesions improved margin analysis, conspicuity, and image quality compared to conventional ultrasound," Clin. Imaging., vol. 25, pp.379-384, 2001.

[9] J.F. Krücker, C.R. Meyer, G.L. LeCarpentier, J.B. Fowlkes and P.L. Carson, "3D spatial compounding of ultrasound imaging using image-based nonrigid registration," Ultrasound med. Biol., vol. 26, pp.1475-1488, 2000.

[10] A. Moskalik, P.L. Carson, C.R. Meyer, J.B. Fowlkes, J.M. Rubin and M.A. Roubidoux, "Registration of 3-dimensional compound ultrasound scans of the breast for refraction and motion correction," Ultrasound Med. Biol., vol. 21, pp.769-778, 1995.

Technical Note

Diffusion Tensor Imaging of Kidneys With Respiratory Triggering: Optimization of Parameters to Demonstrate Anisotropic Structures on Fraction Anisotropy Maps

Masako Kataoka, MD, PhD,[1,2*] Aki Kido, MD, PhD,[3] Akira Yamamoto, MD, PhD,[4] Yuji Nakamoto, MD, PhD,[1] Takashi Koyama, MD, PhD,[5] Hiroyoshi Isoda, MD, PhD,[1] Yoji Maetani, MD, PhD,[1] Shigeaki Umeoka, MD,[6] Ken Tamai, MD,[1] Tsuneo Saga, MD, PhD,[7] Nobuko Morisawa, MD,[1] Susumu Mori, PhD,[8] and Kaori Togashi, MD, PhD[1]

Purpose: To demonstrate the feasibility of diffusion tensor imaging (DTI) of kidneys with respiratory triggering, and determine the optimal imaging parameters for fraction anisotropy (FA) maps.

Materials and Methods: DTI of kidneys from 16 healthy volunteers was performed using a 1.5T scanner. Five different sequences with different parameters including respiration-triggered acquisition or multiple breath-holding, slice thicknesses of 3 or 5 mm, and different numbers of signal averaging and b values were compared. FA and apparent diffusion coefficients (ADCs) of the cortex and medulla were measured. Measurement error within the same and repeated examination was examined using within-individual standard deviation (Sw).

Results: FAs of the renal cortex were lower than the medulla (mean value of a sequence ranging 0.148–0.224, 0.433–0.476) and the ADCs of the cortex were higher than the medulla ($2.26–2.69 \times 10^{-3}$ mm^2/s, $1.77–2.19 \times 10^{-3}$ mm^2/s) in all sequences ($P < 0.001$). The renal cortex–medulla difference was the largest, with respiratory triggering including a 3-mm slice thickness, three signal averages,and a b-value = 0, 200, or 400 s/mm^2 ($P < 0.001$). Sw tended to be smaller in the sequence with a b-value of 400 s/mm^2.

Conclusion: DTI of kidneys with respiratory triggering is feasible with excellent cortex–medulla differentiation.

Key Words: DTI; kidney; respiratory triggering; fractional anisotropy; apparent diffusion coefficient
J. Magn. Reson. Imaging 2009;29:736–744.

DIFFUSION WEIGHTED IMAGING (DWI) of the kidneys is feasible to assess renal failure (1) and conditions associated with kidney transplantation (2) using the apparent diffusion coefficient (ADC). Most of the protocols use diffusion gradients in three orthogonal directions that are subsequently averaged to minimize the effect of anisotropy. However, considering the radially oriented tubular structure of the kidneys, averaging multiple gradients might also decrease information on anisotropic structures, as suggested by previous studies (3–6).

Tissue anisotropy can be evaluated using diffusion tensor imaging (DTI), which enables the measurement of diffusion anisotropy by analyzing water diffusion in different directions. DTI has been widely used in brain neural tractography (7). Since DTI requires several (usually six or more) gradient pulses to assess tissue anisotropy, it involves a longer scanning period and is much more difficult for applications to abdominal organs than DWI.

The kidney may be an ideal candidate for DTI compared with other abdominal organs because it does not contain air, and the renal medulla has a radially oriented architecture. In fact, Ries et al (4) obtained DTI sequences using the single breath-holding (BH) technique and demonstrated the anisotropic structure of

[1]Department of Diagnostic Imaging and Nuclear Medicine, Graduate School of Medicine, Kyoto University, Kyoto, Japan.
[2]Department of Radiology, University of Cambridge, Addenbrooke's Hospital, Cambridge, United Kingdom.
[3]Department of Radiology, Katsura Hospital, Kyoto, Japan.
[4]Department of Radiology, Kyoto City Hospital, Kyoto, Japan.
[5]Department of Radiology, Kyoto University Hospital, Kyoto, Japan.
[6]Department of Radiology, Japan Red Cross Society Wakayama Medical Center, Wakayama, Japan.
[7]Molecular Imaging Center, National Institute of Radiological Sciences, Chiba, Japan.
[8]Center of Magnetic Resonance Microimaging Johns Hopkins University.
Contract grant sponsor: Ministry of Education, Culture, Sports, Science and Technology, Japan; Contract grant number: 16209035.
*Address reprint requests to: M.K., Department of Radiology, University of Cambridge, Box 219, Level 5, Addenbrooke's Hospital, Hills Road, Cambridge, CB2 2QQ, UK. E-mail: makok@kuhp.kyoto-u.ac.jp
Received October 9, 2006; Accepted October 29, 2008.
DOI 10.1002/jmri.21669
Published online in Wiley InterScience (www.interscience.wiley.com).

the kidney on fractional anisotropy (FA) maps. This technique was recently applied to renal cell carcinoma and the structural organization of the tumor was successfully detected (8), suggesting the potential for DTI to reveal pathological alterations in renal architecture. This method reduces misregistration caused by motion. However, it has a limited acquisition time during one BH. To overcome this limitation, respiratory-triggered acquisition or acquisition with the multiple BH technique can be used. These two techniques allow us to increase the image acquisition time. This study aimed to demonstrate that DTI of the kidneys is feasible with respiratory-triggered or multiple BH, and to determine the best imaging parameters for FA maps. To achieve these aims, we: 1) calculated the differences in FA/ADC values among the different sequences, and compared them with those reported by others; 2) measured the cortex–medulla differences in FA maps; and 3) assessed the intraindividual variability for FA and ADC values among the different sequences.

MATERIALS AND METHODS

Study Population

The institutional ethics committee approved our protocols and written informed consent was obtained from all volunteers before entering the study. The study population consisted of 17 healthy volunteers (age range, 22–44 years old; mean age, 34 years old; 14 males and 3 females) who had no previous or current renal disease, hypertension, or other vascular diseases, and no abnormal findings of the kidneys on magnetic resonance imaging (MRI) (except for simple cysts less than 1 cm). No specific preparation including fasting, drinking, and injection of antiperistaltic agents was undertaken prior to MRI examination.

MRI

MRI was performed using a 1.5T scanner (Symphony: Siemens, Erlangen, Germany) with a maximum gradient capability of 30 mT/m and a slew rate of 120 T/m/s. A combination of an anterior and posterior six-channel-phased array body coil was used.

First, T2-weighted half-Fourier rapid acquisitions with relaxation enhancement or RARE-sequence (HASTE; Siemens) axial and coronal to the body axis were obtained for morphological evaluation. Then, coronal DWI with respiration-triggered acquisition or multiple BH (Table 1) were obtained with echo-planar imaging. Initially, we determined a baseline sequence (sequence 1), then we modified the b-value, number of averaging per one continuous data acquisition, method of multiple acquisition (respiratory triggering or multiple BH) or slice thickness to develop four different sequences. The following parameters were common to all five sequences: section thickness, 3 or 5 mm; intersection gap, 1 mm; field of view (FOV), 320 × 320 mm or 350 × 350 mm (adjusted according to the body size of the volunteer and large enough to avoid aliasing artifacts); matrix size; 128 × 128; voxel size, 2.5 × 2.5 × 3 or 5 mm (2.7 × 2.7 × 3 or 5 mm when a FOV of 350 mm was used); bandwidth, 2056 (Hz/Pz); diffusion direction, 6 orientations plus one null; and slice number, 5. A reduction factor for parallel imaging using GRAPPA (generalized autocalibrating partially parallel acquisitions with a reduction factor of 2) was employed (9). Fat saturation was used to avoid chemical shift artifacts.

Table 1
Parameters of the Five Different Sequences for Coronal DW MRI

	Acquisition technique	Slice thickness (mm)	TR/TE (ms)	Nos. of signal averagings	Nos. of series	b value (s/mm²)
1	resp. trig	3	2000/74	3	4	0,200
2	resp. trig	3	2000/74	3	4	0,*400*
3	resp. trig	3	2000/74	*1*	*10*	0,200
4	resp. trig	*5*	2000/74	3	4	0,200
5	*multiple BH*	3	*1000*/74	*1*	*10*	0,200

DW, diffusion-weighted; TR, repetition time; TE, echo time; no., number; resp. trig, respiratory triggered; multiple BH, multiple breath-holding.
Parameters common to all five sequences include: FOV, 320 × 320 (or 350 × 350) mm; matrix size, 128 × 128; bandwidth, 2056 (Hz/Pz); diffusion direction, 7; and slice number, 5.
Values in italics are the parameters different from the baseline sequence (sequence 1: top row).

For respiration-triggered acquisition, a belt-type sensor was wrapped around the abdomen to detect motion of the abdominal walls. Images were obtained in the expiratory phase. A trigger delay of 100 msec with a threshold of 20% was used. This trigger delay period was considered to be the best parameter based on a pilot study using four volunteers (not included in the current study population) with various delay timings and thresholds. Dual triggering of respiration and pulses was also attempted but was not used in the actual comparison study due to the long acquisition time and high failure rate.

The parameters for the baseline sequence (sequence 1) were as follows: repetition time (TR), 2000 msec; echo time (TE), 74 msec; slice thickness, 3 mm; bandwidth, 2056 (Hz/Pz); number of signal averaging, 3; number of series repeated, 4 times; b value, 0 and 200 s/mm^2. In sequence 2, the maximum b-value was modified to 400 s/mm^2 while the other parameters remained the same as in sequence 1. In sequence 3, the number of signal averaging per one acquisition was reduced to 1 but the number of repeated series was increased to 10. In sequence 4, only the slice thickness was increased to 5 mm while the other parameters were kept the same as in sequence 1 (Table 1).

In sequence 5, multiple BH acquisitions were used. One image was obtained per one BH, and the total number of BHs was fixed at 10. Following the instructions by the MR operator, the volunteers were asked to breathe out, and hold their breath to allow for a 15-second scanning time. The interval between one BH acquisition and the next acquisition was not fixed, and was adjusted so that the volunteers felt comfortable. The TR was shortened to 1000 msec to fit within an acquisition time of 15 seconds. TE was maintained at 74 seconds, as in the other sequences. Other parameters, including FOV and bandwidth, were kept the same as in the other sequences.

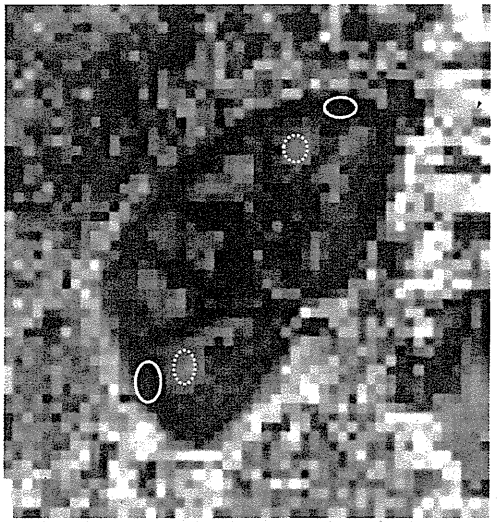

Figure 1. Representative locations of ROIs for the cortex (white circle) and medulla (white dotted circle) at the upper and lower pole of the right kidney are shown. The same ROI were copied to the ADC map to measure the ADC values.

Coronal T2-weighted images were obtained between DWI trials, with the same slice position and FOV to check for any pathological abnormalities.

In the actual scanning, the order of the five different DWI sequences was randomized to avoid systematic bias. The examination time of each sequence was also recorded.

Image Analysis

All DWI were visually reviewed by one of the authors to assess whether the MRI quality was good enough to measure FA and ADC values. DTI datasets were transferred to a workstation and processed using the DtiStudio software (v. 2.3) to obtain FA maps, color maps, and ADC maps. This software is a DTI processing program running on Windows and is designed for tensor calculation, color mapping, fiber tracking, and 3D visualization. To increase the signal-to-noise ratio (SNR), all the acquired series (four series in sequences 1, 2, and 4, and 10 series in sequences 3 and 5) were used for analysis. In sequence 5, 10 series of images obtained in 10 consecutive BH were averaged and used in the analysis. Offline registration was not used for respiratory triggered sequences or the BH sequence, as it did not improve image quality. One of five slices was carefully selected to include the maximal renal area and to exclude visible renal vessels. Care was taken to avoid slices with small renal cysts.

Two different regions of interest (ROIs), as large as possible and not less than 10 pixels were placed over the cortex and medulla on the upper and lower pole of the right kidney by one of the authors (Fig. 1). ROIs were carefully selected to avoid areas of aliasing artifacts when they appeared on images. The ROI of the medulla was carefully placed to avoid visible vessels and renal pelvic structure. HASTE images were used as reference images to check anatomical structure. Signal intensity and standard deviations (SDs) were measured. ROIs on FA maps were copied onto the same locations on the ADC maps to measure the ADC values. To reduce variability, the average of the two FA measurements from two ROIs in the cortex in one kidney was used as a representative cortical FA value. The same was applied to the medullary FA value, cortical ADC value, and medullary ADC value. The mean, SDs, and standard errors of the mean (SEM) of the FA and ADC values among the 16 volunteers were calculated for the cortex and medulla. The FA difference between the cortex and medulla on the FA maps was computed to quantify the cortex–medulla contrast.

The same measurement was also performed for the left kidney. As none of the volunteers had conditions affecting a unilateral kidney, measurements of left kidney were used to investigate reproducibility in the same examination. In addition, images of sequence 1 taken on a different date were available for five volunteers during the pilot study and they were used to examine the reproducibility of the repeated examinations. The interval between the two examinations was 37–175 days.

In addition to ROI measurement, 5-grade qualitative evaluation of FA maps and ADC maps from each sequence was scored by two of the authors in consensus; 1, not evaluable; 2, poor (cortex–medulla difference is not visible); 3, moderate (cortex–medulla difference is visible but not clear); 4, good (reasonable cortex–medulla difference); 5, excellent (clear cortex–medulla difference).

Statistical Analysis

The FA and ADC values for each sequence did not follow the normal distribution. Therefore, differences in FA and ADC values between the cortex and medulla in each sequence were compared using Wilcoxon's rank-sum test.

Repeated-measures analysis of variance was used to examine the effect of variable sequences on the cortex–medulla differences of FA. To further investigate the differences, a post-hoc analysis was performed with Dunnett's *t*-test using sequence 1 as control.

As a marker of measurement error or reproducibility of the value from each individual, the intraindividual (organ) variabilities of FA and ADC values were examined by calculating the within-individual standard deviation (Sw) (10). Sw was calculated based on the two values from two ROIs as follows:

V = variance of the two values (FA or ADC) from two ROIs in the cortex or medulla.
Sw = (average of V in all volunteers)$^{1/2}$

Measurement error within the same kidney was examined by Sw using two ROIs within the right kidney. Measurement error within the same individual was also examined by Sw using ROIs of the upper poles from the right and left kidneys obtained from the same examinations. In addition, the reproducibility of the measurement was examined by Sw using ROIs of the upper

Table 2
FA and ADC Values of the Renal Cortex and Medulla

	FA						ADC ($\times 10^{-3}$ mm^2/s)						Total acquisition time (min)
	Cortex			Medulla			Cortex			Medulla			
	mean	SD	SE	mean	SD	SE	mean	SD	SE	mean	SD	SE	
1	0.167	0.020	0.005	0.476	0.040	0.010	2.64	0.22	0.05	2.00	0.20	0.05	6.5
2	0.148	0.012	0.003	0.450	0.034	0.009	2.26	0.14	0.04	1.82	0.19	0.05	6.6
3	0.195	0.021	0.005	0.468	0.058	0.015	2.58	0.14	0.04	2.03	0.17	0.04	8.5
4	0.182	0.031	0.006	0.433	0.040	0.014	2.69	0.23	0.04	2.19	0.21	0.05	7.0
5	0.224	0.024	0.006	0.463	0.054	0.010	2.42	0.16	0.06	1.77	0.21	0.05	6.4

FAs of the renal cortex were lower than medulla and the ADCs of the cortex were higher than medulla in all sequences ($P < 0.001$).
FA, fractional anisotropy; ADC, apparent diffusion coefficient; SD, standard deviation of each measurement from data of 16 volunteers (interindividual standard deviation); SE, standard error of the mean of each measurement from data of 16 volunteers (interindividual standard deviation).

poles of the right kidneys obtained from repeated examinations.

RESULTS

One volunteer was excluded from the analysis due to severe motion artifacts; thus, only 16 subjects were included in the analysis.

The average time for each examination was 6.5–7.0 minutes for respiratory-triggered acquisition with three signal averages repeated four times (sequences 1, 2, and 4), 8.5 minutes for respiratory-triggered acquisition with one signal averaging repeated 10 times (sequence 3), and 6.4 minutes for 10 BH acquisitions (sequence 5).

Table 2 shows the FA values and ADC values obtained with the five different sequences. FA of the renal cortex ranged from 0.148 to 0.224, and that of the medulla ranged from 0.433 to 0.476. ADC of the cortex ranged from 2.26 to 2.69 $\times 10^{-3}$ mm^2/sec, and that of the medulla ranged from 1.77 to 2.19 $\times 10^{-3}$ mm^2/sec. FAs of the renal cortex were lower than the medulla and the ADCs of the cortex were higher than the medulla in all sequences ($P < 0.001$). Both the FA and the ADC values tended to be smaller in sequence 2.

Figure 2 shows the differences in FA values between the cortex and medulla (mean value and standard deviation). Repeated-measures analysis of variance revealed that the different sequences affected the size of the cortex–medulla differences (test of within-subjects effects; Huynh–Feldt F-value, 8.39; $P < 0.001$). To further investigate the differences, a post-hoc analysis was performed with Dunnett's *t*-test using sequence 1 as the control. Compared with the baseline sequence 1, sequences 4 and 5 showed significantly smaller cortex–medulla differences ($P < 0.001$ and $P = 0.001$, respectively). Sequence 2 revealed a cortex–medulla difference similar to that in sequence 1. Sequence 3 showed a cortex–medulla difference smaller than that in sequence 1 but the difference was not significant ($P = 0.075$). The distribution of FA and ADC values in each sequence is shown in Fig. 3.

Table 3 shows the intraindividual Sw using two ROIs within the right kidney. Sw ranged from 7%–18% of the mean value. Sw tended to be smaller in sequence 2, followed by sequence 1 for the FA values of the cortex and medulla, and for the ADC values of the cortex and medulla. In contrast, sequence 5 tended to show the largest Sw.

Table 4 shows the intraindividual Sw using ROIs of the upper pole of right and left kidneys within the same examination. Sw ranged from 7%–30% of the mean value. Sw tended to be smaller in sequences 1 and 2, for the FA values of the cortex and medulla, and the ADC values of the cortex and medulla.

Repeatability was examined by intraindividual Sw using ROIs of upper poles of right kidneys obtained from repeated examinations in five of the volunteers for sequence 1. Sw for the FA values of the cortex and medulla, and ADC values of the cortex and medulla were 0.020 (percentage of Sw per mean values: 12.1%), 0.075 (15.1%), 0.23 (8.6%), and 0.18 (9.6%), respectively.

In qualitative evaluation of the FA maps, sequences 1 and 2 scored highest, followed by sequence 4; sequence 5 had the lowest score. The difference in scores among sequences was smaller for the ADC maps than for FA maps. Again, sequences 1 and 2 scored highest (Table 5).

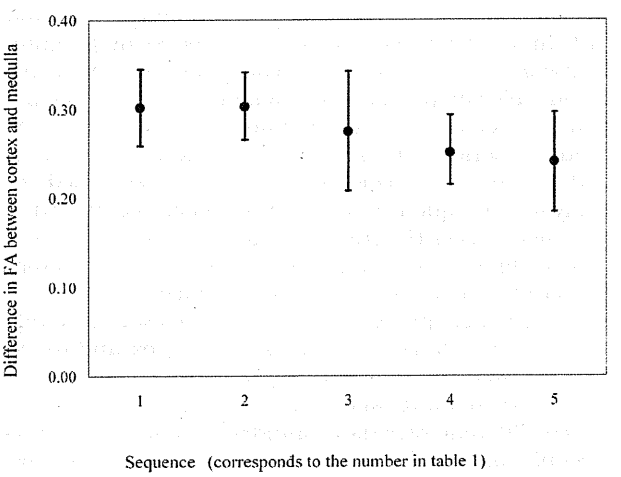

Figure 2. Differences between the cortex and medulla on FA maps in sequences 1–5 ($n = 16$). Results are expressed as means (black dots) and standard deviations (error bars). Numbers on the X-axis correspond to sequences 1–5 according to Table 1. The Y-axis reveals the different FA values between the cortex and medulla.

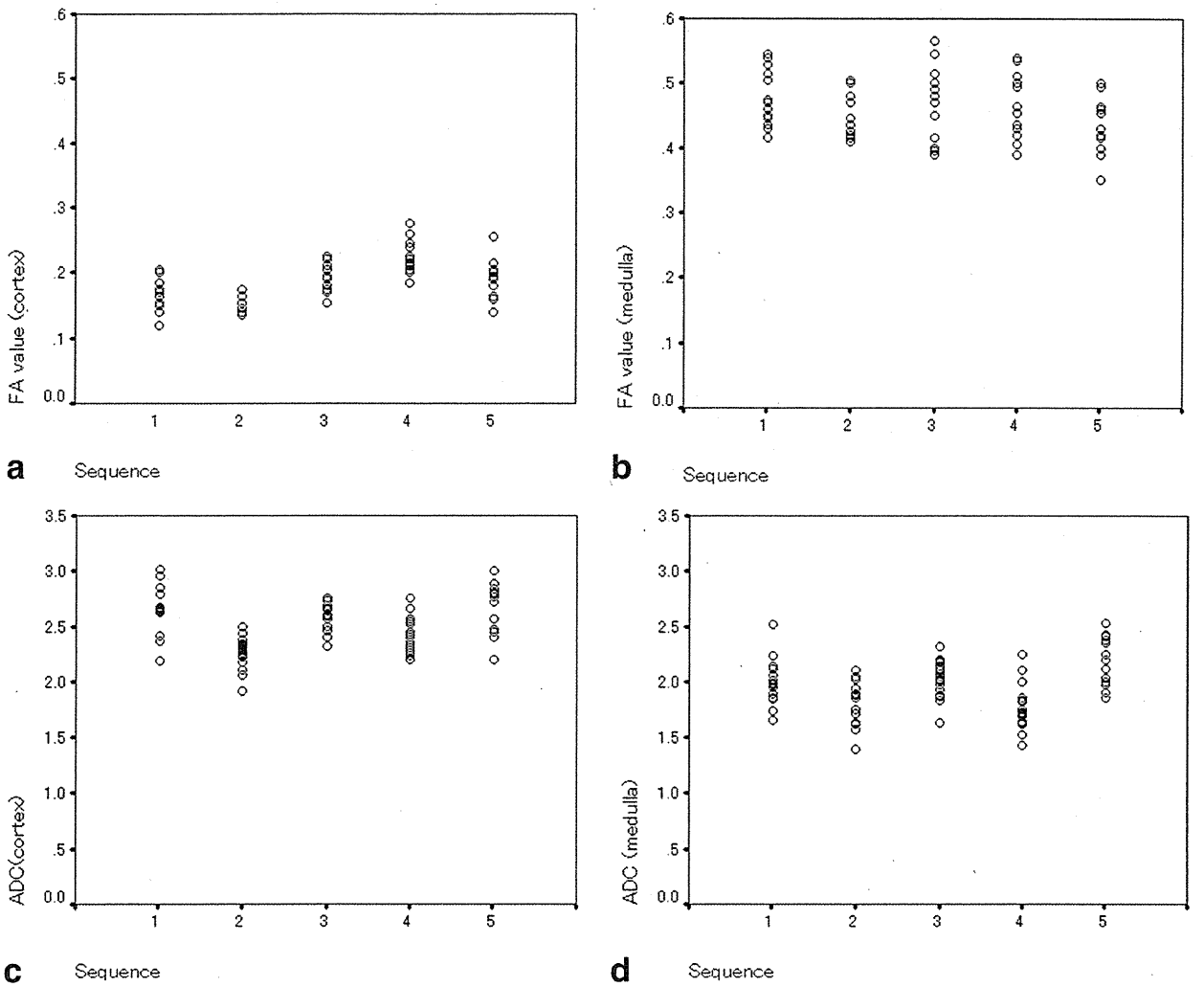

Figure 3. Scatterplot of distributions of FA values in cortex **(a)**, medulla **(b)**, and ADC values in cortex **(c)** and medulla **(d)** in sequences 1–5.

For 10 volunteers smaller FOVs were used (320 × 320 mm) and for six volunteers larger FOVs were used (350 × 350 mm). There was no significant difference in FA and ADC values and qualitative scoring between the two groups. Representative images are shown in Fig. 4.

DISCUSSION

This study demonstrated that DTI of the kidneys with respiratory-triggered acquisition was feasible, with excellent cortex–medulla differentiation. DTI with sufficiently good image quality was successfully obtained in ≈94% (16 of 17 volunteers) of the subjects. Combining the results of the FA and ADC values, cortex–medulla contrast, measurement error (reproducibility), and qualitative evaluation, sequences 1 and 2 provide the best protocol. Sequence 4 scored highly for image quality but measurement variability tended to be larger than for sequences 1 and 2.

Only a few studies have reported the use of DTI for abdominal organs (4,11). Ries et al used single-shot echo-planar sequences with pulse-triggering. Low SNR is a fundamental problem of poor image quality in single BH acquisition, although the short acquisition time and fewer motion artifacts are advantages of this technique. Our current study showed the feasibility of DTI for the kidneys using respiratory-triggered acquisition. DTI with multiple BH also produced slightly lower FA and similar ADC values, but within-individual standard deviations tended to be larger than those obtained with respiratory-triggering acquisition. This could be explained by variations in position among the 10 repeated BHs, which might have also led to a decrease in cortex–medulla contrast.

Misregistration of the kidney during respiratory-triggered acquisition might still exist owing to movements of the kidney during respiration. We used a belt-type sensor to detect respiratory motion, but the movements of the kidneys associated with respiration are mainly in a cranio–caudal direction, and do not always coincide with the abdominal wall movements. Ideally, navigator-echo-type respiratory triggering that monitors dia-